

The X-ray Halo of GX 13+1

Randall K. Smith, Richard J. Edgar

Smithsonian Astrophysical Observatory, 60 Garden St., Cambridge, MA 02138

rsmith,redgar@cfa.harvard.edu

and

Richard A. Shafer

Code 685, Laboratory for Astronomy and Space Physics, NASA Goddard Space Flight
Center, Greenbelt, MD 20771

richard.shafer@gsfc.nasa.gov

Received _____; accepted _____

ABSTRACT

We present observations of the X-ray halo around the LMXB GX 13+1 observed with the *Chandra* X-ray telescope. The halo is due to small-angle scattering by interstellar dust grains, and we use it to diagnose the likely line-of-sight position and size distribution of the grains. We find two unexpected results: first, there is an unexpected energy dependence so that the halo is stronger at high energies than theory predicts, and secondly that the halo far off-axis is stronger than most dust grain models predict. Despite these surprises, we are able to conclude that our data does not agree with “fluffy” dust models that earlier X-ray halo observations have supported. In addition, models of an additional “large” dust grain population seen in the local ISM are not supported by these data

Subject headings: dust — scattering — X-rays: binaries — X-rays: ISM

1. Introduction

X-ray halos are created by the small-angle scattering of X-rays passing through dust grains in the interstellar medium. The spectral and spatial characteristics of X-ray halos are determined by the size, line of sight distribution, and composition of dust grains, with a bias towards larger dust grains which are the primary sites for X-ray scattering. These larger grains hold much of the mass that is in dust grains and they are difficult to detect in other wavebands. In this paper, we will describe how observations of the halo around GX 13+1 can be used to place limits on dust grain models, specifically on the population of larger grains.

GX 13+1, a low-mass X-ray binary (LMXB), is a bright highly-absorbed X-ray source. IR spectral observations by Bandyopadhyay *et al.* (1999) show that the secondary star

is likely a K5 giant, and they calculate a distance of 7 ± 1 kpc for the system. GX 13+1 has been classified as an atoll source (Hasinger & van der Klis 1989), although it belongs to a small subclass of atoll sources that are persistently bright. The X-ray halo around GX 13+1 was first described by Catura (1983), who used *Einstein* HRI data and measured a total halo flux equal to 0.18 ± 0.02 of the source flux in the HRI band (0.1-6 keV). However, Catura noted that systematic uncertainties in the observation probably lead to an underestimate of the halo strength. Subsequently, Mauche & Gorenstein (1986) used *Einstein* IPC observations of GX 13+1 to measure a halo fraction of 0.17 ± 0.01 in the IPC band (0.1-6.4 keV). In 1995, Predehl & Schmitt measured the X-ray halo of GX 13+1 using only 47 seconds of observations from the ROSAT All-Sky Survey. They found a much brighter X-ray halo, 0.37 ± 0.04 of the source flux in the PSPC band (0.08-2.9 keV). The discrepancy between the *Einstein* and *ROSAT* observations has not been discussed, but is likely due to the different energy bands of the instruments.

Measurements of X-ray halos have been used to place limits on the dust grain density (Mathis *et al.* 1995), as well as the dust size distribution (Witt, Smith & Dwek 2001). The *Chandra* observations provide the far higher angular and energy resolution than has been available, and we will discuss what limits can be placed on these values using this high-quality data set. However, we are limited by the instrumental calibration, which is only incomplete in regards to the far off-axis PSF ($> 100''$) that is the predominant background to the X-ray halo. We partially compensated for this by using calibration data from 3C273 directly.

2. Theoretical Background

X-ray halos are formed when X-rays emitted by bright source scatter while passing through dust grains in the interstellar medium. The theory was first discussed in an

astrophysical context by Overbeck (1965), and has since been refined by a number of authors (Mauche & Gorenstein 1986; Mathis & Lee 1991; Smith & Dwek 2000). We briefly review the theory here.

The fundamental quantity is the differential scattering cross section $d\sigma/d\Omega$, which can be calculated using either the exact Mie solution or the Rayleigh-Gans (RG) approximation; see Smith & Dwek (2000) for a discussion. The RG approximation is derived by assuming each volume dV in the dust scatters X-rays via Rayleigh scattering, and then integrating the result over the grain volume. Analytically, it can be written as

$$\frac{d\sigma(\theta_{\text{sca}})}{d\Omega} = 1.1 \text{cm}^2 \text{sr}^{-1} \left(\frac{2Z}{M} \right)^2 \left(\frac{\rho}{3 \text{g cm}^{-3}} \right)^2 a_{\mu\text{m}}^6 \left(\frac{F(E)}{Z} \right)^2 \Phi^2(\theta_{\text{sca}}) \quad (1)$$

where a is the grain radius, Z is the mean atomic charge, M the mean atomic weight (in amu), ρ the mass density, E the X-ray energy in keV, $F(E)$ the atomic scattering factor (Henke 1981), θ_{sca} the scattering angle, and $\Phi^2(\theta_{\text{sca}})$ the scattering form factor (Mathis & Lee 1991). For homogeneous spherical grains, the form factor is given by

$$\Phi^2(\theta_{\text{sca}}) = 3(\sin u - u \cos u)/u^3 \quad (2)$$

where $u = 4\pi a \sin(\theta_{\text{sca}}/2)/\lambda \approx 2\pi a \theta_{\text{sca}} E/hc$.

Smith & Dwek (2000) showed that the RG approximation will overestimate the total scattering if the energy of the X-rays (in keV) is not substantially larger than the size of the dust grains (in μm), and suggested 2 keV as a minimum energy. The spectrum of GX 13+1 peaks beyond 2 keV, so we will use the RG approximation in this paper.

The total X-ray halo can then be calculated by combining the scattering cross section with the line of sight geometry to get (considering single scatterings only) the halo surface brightness at angle θ :

$$I_{\text{sca}}(\theta) = F_X N_H \int dE S(E) \int dan(a) \int dx \frac{f(x)}{(1-x)^2} \frac{d\sigma}{d\Omega} \quad (3)$$

where F_X is the total source flux, N_{H} is the hydrogen column density, $S(E)$ is the (normalized) X-ray spectrum, and $n(a)da$ is the dust grain size distribution. Here $f(x)$ is the density of hydrogen at distance xD from the observer divided by the line of sight average density, where D is the distance to the source (Mathis & Lee 1991).

Of course if the column density is sufficiently large, individual X-rays may be scattered multiple times. Mathis & Lee (1991) showed that for $\tau_{\text{sca}} > 1.3$, multiple scatterings dominate over single scattering, tending to broaden the halo. The scattering cross section depends upon the X-ray energy and the dust model; Table 1 of Mathis & Lee (1991) shows that $\sigma_{\text{sca}} = 9.03 \times 10^{-23} E_{\text{keV}}^{-2}$ for diffuse dust models such as Mathis, Rumpl & Nordsieck (1977; MRN) or Draine & Lee (1984). For $N_{\text{H}} \approx 2.9 \times 10^{22} \text{ cm}^{-2}$ (see §3.1), this corresponds to $\tau_{\text{sca}} = 2.6 E_{\text{keV}}^{-2}$. Above 2 keV, multiple scattering will not be a significant effect. Below 2 keV, we can expect that the RG approximation will somewhat overestimate the total halo intensity and the single scattering approximation will underestimate the radial extent of the halo.

3. Observations and Analysis

GX 13+1 was observed with the *Chandra* ACIS-I array (chips I0-3, S2, S3) for 9.74 ksec on August 7th, 2000. GX 13+1 was at the aimpoint, and as can be seen in Figure 1, a bright halo was observed although as expected the source itself suffered from severe pile-up. We processed the data using the *Chandra* data system software version R4CU5UPD14.1, and used CIAO version 2.2 for our analysis.

The ACIS-I CCDs were damaged early in the *Chandra* mission by low-energy protons. As a result the energy resolution decreased; at 1.5 keV, the FWHM on ACIS-I3 now varies from ~ 100 eV to ~ 150 eV, depending on the row number. Based on this resolution and

the quantity of data, we decided to bin the observations into 200 eV segments.

3.1. Spectral Analysis

The X-ray halo is directly proportional to the source spectrum, so any uncertainties in the spectral analysis will affect the halo analysis. Ideally, the spectral measurement would be high-resolution and contemporaneous; for this observation, however, we have only the ACIS-I data. In CCD detectors like the ACIS-I, pileup occurs when two or more photons impact the same or adjacent pixels within a single frame. This can mimic a single photon with energy equal to the sum of the photon energies, or it can change the event “grade” from a good X-ray detection (grades 0, 2, 3, 4, or 6) to a rejected likely cosmic-ray event (grade 7) (Chandra Proposers’ Observatory Guide, Rev. 4.0, p 106). In GX 13+1, the core pileup was large enough that all photons within a $3''$ of the source migrated to grade 7 and were automatically rejected, while regions slightly further off-axis were heavily contaminated by pile-up.

Despite this, the source spectrum can be relatively easily extracted from the “transfer streak,” which appears as a line connecting the detector aimpoint and the chip readout in Figure 1. During the 42 ms frame transfer of the ACIS CCDs, X-rays from the source continue to arrive at the aimpoint and are as a result “mis-positioned” along the axis of the transfer by the *Chandra* processing software. In 9.74 ksec of observing, the ACIS spends ~ 128 seconds doing frame transfer. We extracted $\sim 31,000$ events in an 11×908 pixel strip around this streak (avoiding the near-aimpoint region which will be affected to a lesser degree by pileup). We assumed all the events originated on-axis in calculating the detector response (M. Bautz 2001 private communication).

Other non-contemporaneous X-ray observations of GX 13+1 exist. GX 13+1 is

regularly observed by the RXTE All-sky Monitor (ASM), although it was not observed for a period of ~ 10 days surrounding the Chandra observation. The long-term ASM lightcurve shows that the luminosity in the 1.3-12.1 keV bandpass is relatively constant, with intrinsic variations of $\sim 50\%$ (Homan *et al.* 1998). GX 13+1 was also observed by ASCA for 18.8 ksec in September 1994. We extracted the GIS data, which have nearly 10^6 counts; the source was blocked out in the SIS detectors. The flux observed by ASCA in the 1-10 keV band is $\sim 25\%$ larger than observed by *Chandra*, likely due to fluctuations in the source itself.

The observed halo intensity at energy E is proportional to the observed source flux at energy E and the column density of dust along the line of sight. To estimate these we fit a range of spectral models and examined the results. Intrinsically, the X-ray spectra of LMXBs vary widely due to the many possible viewing angles and emission mechanisms. We therefore considered a number of different models, following the Christian & Swank (1997) analysis of the X-ray emission for a sample of LMXBs. We used both blackbody and thermal bremsstrahlung models, along with a number of two component models with a blackbody (BB) plus either a thermal bremsstrahlung (TB), power law (PL), or a disk blackbody (DBB; see Mitsuda *et al.* 1984, Makishima *et al.* 1986). In addition, we fit the spectrum using a series of top-hat functions, roughly matching the ACIS-I resolution by using 100 eV spacing from 1-2 keV and 200 eV spacing from 2-4 keV. This approach measures the observed flux (with errors) in each band without reference to any specific model.

All of these models led to a formally acceptable value of χ^2 , due to the low count rate and energy resolution in the transfer streak data. The best-fit column density varied from 1.99 to 4.17×10^{22} cm $^{-2}$ depending on which source model was used. The absorption column density has been measured with other X-ray satellites; Ueda *et al.* (2001) found

$N_{\text{H}} = 2.9 \pm 0.1 \times 10^{22} \text{ cm}^{-2}$ from ASCA GIS and SIS observations, which agrees with the value found by Shultz, Hasinger & Trümper (1989) from EXOSAT ME data. Garcia *et al.* (1992) placed an upper limit of $A_V \lesssim 14.4$ based on measurements in the J, H, and K bands and assuming the spectrum rose no faster than the Jeans tail on a blackbody. Using the conversion from $N_{\text{H}}/A_V = 1.9 \times 10^{21} \text{ cm}^{-2}/\text{mag}$ (Seward 2000), this is equivalent to $N_{\text{H}} \lesssim 2.7 \times 10^{22} \text{ cm}^{-2}$.

We can also calculate the flux from these models, as shown in Figure 2. The summed top-hat model results in similar fluxes as the different spectral models, and the errors on the top-hat amplitudes are on the same scale as the variations in the spectral models. We will use the top-hat fluxes and errors for the following analysis.

3.2. Imaging Analysis

Measuring the radial profile of GX 13+1 is straightforward. We begin by removing any serendipitous sources from the image. We then make exposure maps and extract images for each energy band to be used. The data are extracted in concentric annuli centered around GX 13+1’s position, and the same is done with the exposure map. To get the intensity of the halo as a function of energy and radius we simply divide the counts in each annulus by the total exposure in that annulus.

We began searching for sources in the field of view using the CIAO tool *celldetect*. Since removing a false source merely reduces the signal to noise slightly, while including a source mistakenly would add a systematic error, we decided to accept any source found with significance greater than 4σ . This resulted in six sources, listed in Table 1. A search using *Simbad* showed no known sources with $10''$ of these positions. The *Simbad* search found 39 objects in the field of view, including stars, IRAS objects, and a supernova remnant

(G13.5+0.2). None of these sources could be seen in the data, although source D is inside the remnant.

The X-ray halo of GX 13+1 fills the ACIS-I field of view, as can be seen in Figure 1. However, the central $3''$ region around the source has no data due to severe pileup. We estimated the true source position by requiring the center to lie on the line defined by the transfer streak and centering using the contours of the data. We then found the position of GX 13+1 to be RA,Dec = 18:14:31.065, -17:09:26.02 (J2000), with an estimated error of $0.3''$. This is $0.3''$ distant from the position measured by Berendsen *et al.* (2000) using radio observations of GX 13+1 with the ATCA. The halo appears to be radially symmetric about the source, as expected from theory and previous observations. We confirmed this by examining the data in various radial bins as a function of polar angle. The data showed no significant variation as a function of angle. We are therefore justified in extracting the radial profile of the X-ray halo by summing the data in annular rings in our selected energy bands.

Pileup substantially affects the central radial bins, so we must determine where it drops off. This is difficult to estimate *a priori*, since pileup can occur not only when two X-rays strike the same pixel within a single frame time, but also when the two X-rays hit adjacent pixels. Depending on the details of the interaction of the X-ray in the CCD, pileup may lead to events not being recognized, or being rejected, or being identified with the wrong energy and/or a modified grade. We therefore estimated the pileup rate phenomenologically by examining the radial profiles of different grade events. When the count rate is low, the ratio of event grades should tend to a constant which depends on the spectrum. In Figure 3(a) we plot the radial profile of good (grade 0,2,3,4, and 6) events, along with the profile of just grade 0 (single-pixel), and grade 6 (four-pixel) events. Figure 3(b) shows the ratio of grade 0 and grade 6 events to the total as a function of radius, along with

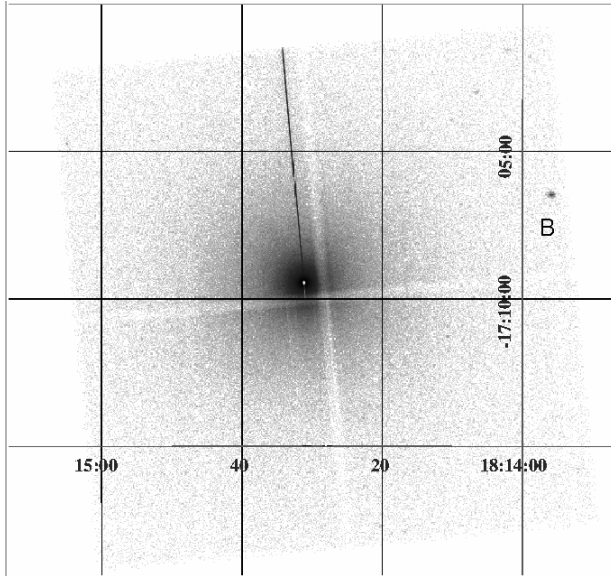


Fig. 1.— *Chandra* ACIS-I image of GX 13+1. The transfer streak can be seen extending from the central source, and the serendipitous source “B” is marked. Also notable are the chip gaps of the ACIS-I array.

Table 1: Serendipitous Source List

Source	RA (J2000)	Dec (J2000)	Net Flux (cts/ksec)
B	18:13:55.833	-17:06:28.09	76.8958
C	18:14:37.346	-17:10:39.70	4.77356
D	18:14:10.560	-17:11:17.01	2.17923
E	18:15:04.775	-17:04:46.79	3.00942
F	18:14:02.059	-17:01:33.98	4.25470
G	18:14:06.447	-17:03:00.61	7.05657

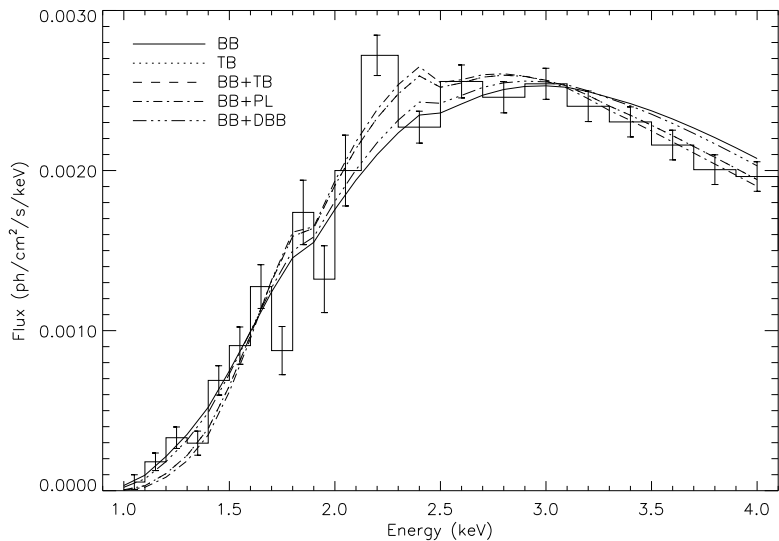


Fig. 2.— Calculated flux from GX 13+1 after fitting data with blackbody (BB), thermal bremsstrahlung (TB), blackbody plus thermal bremsstrahlung (BB+TB), blackbody plus power law (BB+PL) and a blackbody and disk blackbody (BB+DBB) model. The histogram shows the fluxes and errors found using a model consisting of a sum of top-hat functions. Note that despite the wide range of models, the flux in each energy band varies only slightly.

the limiting ratio found far from the source. This is not a perfect estimate of the ratio close to the source since the X-ray halo will have some spectral differences from the source, but we do not expect the difference to be substantial. As Figure 3(b) shows, pileup/grade migration is a noticeable effect even as far as $50''$ from the source. We can derive a similar result analytically as well. According to the *Chandra* proposers’ guide, a pileup fraction of 10% will impact the resulting image or spectrum. Using the 3.2 second ACIS frame time and a poisson-distributed count rate, 10% pileup (or two photons in a single 3×3 pixel grid in one frame) corresponds to a rate of $0.0037 \text{ cts s}^{-1} \text{ pixel}^{-1}$. As Figure 3 shows, this is the rate found within $\sim 20''$ of the source, where the effect of pileup is most severe.

We can now extract the radial profile of the X-ray halo. We divided the dataset into 9 energy bands, spaced every 0.2 keV from 2.0-4.0 keV in order to match the ACIS-I resolution. To effectively use *Chandra*’s angular resolution while also equalizing the number of counts in each annulus, we used 99 log-spaced annuli from $10''$ to $600''$ (plus one from $0\text{-}10''$). After extracting the radial profiles of the data, we then calculated exposure maps for each energy band and used the same annuli to extract the total effective area at each energy and radius. The serendipitous sources were removed both from the data and the exposure maps, so the results are self-consistent. We then divided the radial profile of event data by that of the exposure map to get a result in physical units of photons $\text{cm}^{-2} \text{ s}^{-1} \text{ arcmin}^{-2}$. This approach does not take into account the varying response of the CCDs. On-axis at 1.5 (4.5) keV, the FWHM is ~ 160 (~ 300) eV, while at the chip readouts, it is ~ 80 (~ 130) eV. Due to the physical layout of the ACIS-I CCDs, small off-axis angles are all far from the chip readouts, while large off-axis angles will contain points both near and far from the chip readouts (Chandra Proposers’ Observatory Guide, Rev. 4.0, p. 74, 86). As a result, there will be a systematic effect in the “average” ACIS response as a function of off-axis angle. We used energies between 2-4 keV summed in broad 200 eV bands to minimize these effects.

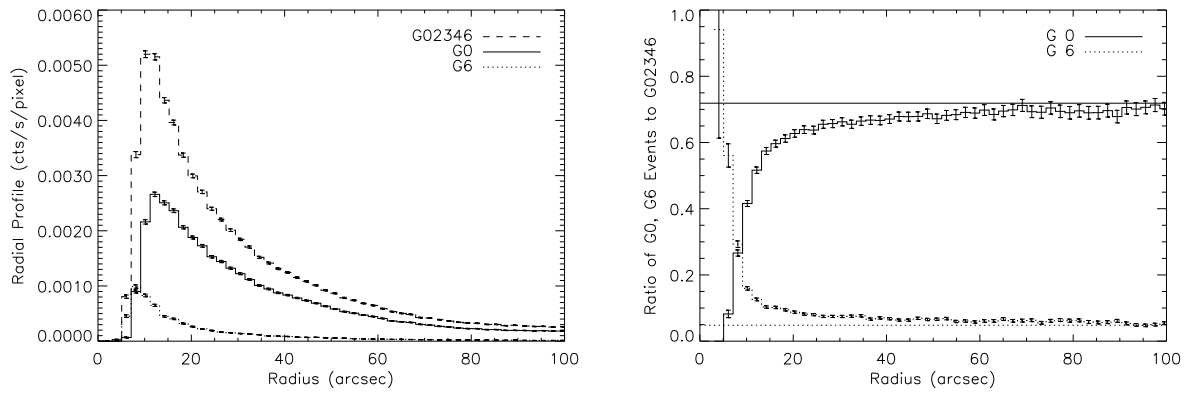


Fig. 3.— (a) The surface brightness of GX 13+1 as a function of radius, including both grade 0, grade 6, and the sum of all “good” grades 0, 2, 3, 4, and 6. Near the source, marginal grade 6 events dominate the flux, while far from the source single-pixel grade 0 events do. (b) The ratio of grade 0 and grade 6 to the sum of all good events, as a function of radius. The horizontal line shows the expected value for grade 0 events far from the source. Within $50''$ of the source, pileup is a noticeable issue.

The final stage of the analysis is to remove the point-spread-function (PSF) of the telescope. The CIAO tool *mkpsf*, although fine for calculating the core of the PSF, is not useful here since we are interested in the PSF 1' or more from the source. In collaboration with the CXC calibration team, we used the *Chandra* raytrace model “SAOsac,” (release as of 9/18/01) which matches the observed core of the PSF well but underestimates the wings of the PSF (T. Gaetz, 2002, private communication). The exact amount of the disagreement depends on the X-ray energy and the off-axis angle; at 500'' it varies from a factor of 2 at 1.5 keV to a factor of 6 at 4.5 keV¹. We also measured the PSF using the calibration observation (obsid 1712) of 3C273 on ACIS-S. This showed a good match to the SAOsac code for $\theta \lesssim 100''$; beyond that the count rate was too low to measure the radial profile. The advantage of this approach is that we can analyze the data identically for both sources, removing many potential systematic errors. We chose 3C273 because it has a low absorption column density, and as an extragalactic source its X-ray halo will intrinsically be weak. The analysis was identical to that done for GX 13+1.

4. Results

GX 13+1's X-ray halo provides a rich data set for deriving properties of dust grains in the interstellar medium. Since the X-ray halo is a function of the size, position, and composition of the dust grains, as well as the source flux and absorption column, we must begin with some assumptions. We first consider the smoothly-distributed dust model, where the dust grain density is constant along the line of sight. We compare three dust grain models: the MRN model, the recent Weingartner & Draine (2001; WD) model, and the “extended” MRN model (hereafter the XMRN model) described by Landgraf *et al.* (2000)

¹Chapter 15 of the XRCF report, <http://hea-www.harvard.edu/MST/simul/xrcf/report/index.html>

and used by Witt, Smith, & Dwek (2001). This model is based on the *insitu* measurements made by *Ulysses* and *Galileo*, and has the same total mass as the MRN model, but extends the MRN size distribution to $2.0\,\mu\text{m}$, with a break at $0.5\,\mu\text{m}$ from a -3.5 power law to -4.0 for larger grains.

In Figure 4 we show our best-fit results at three energies, using the MRN, WD, and the XMRN dust grain models. The only free parameter in these fits is the total dust grain column, which from spectral fits appears to be $N_{\text{H}} \approx 2.9 \times 10^{22}\,\text{cm}^{-2}$. A number of features are immediately apparent in these results. First, the XMRN model is consistently poor, overestimating the halo at small angles and underestimating it at large angles. At 2.1 keV, this could be partially due to the RG approximation breaking down, but RG should be adequate at 3.7 keV where it is clearly a poor fit. Although we cannot completely rule out models with substantial populations of grains larger than $0.25\,\mu\text{m}$, this dataset certainly does not require them. Secondly, although the MRN and WD models clearly represent the gross halo features, there is an excess at large angles that is explained by neither. The excess could be due to multiple dust scattering, but then it should be smaller at higher energies, not larger. This effect is at least partially due to calibration problems. As noted above, we used the SAOsac raytrace model, which does underestimate the mirror scattering at large angles. We tried fits using up to 6 times the SAOsac PSF and still found a small excess at large angles, although it was much reduced. If the effect is real, it could be due to small dust grains or grains far from the source, as large dust grains (or additional grains near the source) cause an increase at small angles.

The third feature is that the column density N_{H} increases as the energy increases for all our models (see Figure 5). The statistical errors on N_{H} are of order 1%, so the effect must be either due to calibration problems or to an astrophysical source. This trend with energy is at likely at least partially due to calibration, given the known disagreement between SAOsac

and the ground calibration results. We experimented with this by limiting our fits to the region between $50 - 100''$ off-axis, where pileup was minimal and we could calibrate the PSF using 3c273. The same trend with energy was apparent, although much less pronounced. For example, the best-fit N_{H} for the MRN model varied from $2.3 - 2.8 \times 10^{22} \text{ cm}^{-2}$ instead of the $2.4 - 3.5 \times 10^{22} \text{ cm}^{-2}$ seen for the fits over the entire $50 - 600''$. If this trend is even partially real, it is difficult to understand. The dust composition, for example, is unlikely to cause it. The X-ray scattering is caused by interactions with electrons in the grain; if these electrons have binding energies close to the energy of the X-rays, absorption could occur. However, the electron binding energies for the L and M shell electrons of C, O, Mg, Si, and Fe are all substantially below 2 keV, so these electrons should all behave as free electrons in a composition-independent fashion. The few K shell electrons which do have energies near 2 keV (or 6.4 keV in the case of iron) contribute relatively little to the total scattering.

4.1. Molecular clouds

We have assumed that the dust grains were smoothly distributed along the line of sight (*i.e.* $f(x) \equiv 1$). We can relax this restriction and assume instead that dust grains are found in clumps along the line of sight. This is probably a more realistic model, as the sightline to GX 13+1 crosses two or three spiral arms (Caswell & Haynes 1987; Taylor & Cordes 1993), spaced at about 20%, 40%, and 60% of the distance to GX 13+1. In Figure 6 we show the profiles for E=2.1, 2.9, and 3.7 keV along with fits using MRN dust and four “clouds” placed at 20%, 40%, 60%, and 80% of the distance to GX 13+1. The amount of dust in each cloud was allowed to vary independently, but was fixed to be the same value for each X-ray energy. These models show one result similar to the smoothly-distributed dust case: as the energy increases, the model tends to underpredict the total halo. Since the amount of dust in each cloud was not allowed to vary with energy, the best-fit result exceeds the

data at low energies and underestimates at high energies. In addition, the total amount of dust used (measured by the N_{H}) is similar to the smoothly distributed models.

We also experimented with fits using a single cloud and could not find an adequate fit for any dust model. These fits show that two clouds, however, fit the data as well as the smoothly-distributed case. One cloud must be near the source to reproduce the scattering seen at $\theta < 100''$ and the second cloud must be near the observer to get the more extended scattering. The clouds 40% and 60% of the distance to GX 13+1 do not appear to be needed by the model. Our results therefore suggest that the nearest spiral arm contributes substantial dust, along with material near the Galactic center.

5. Conclusions

The high angular resolution of the *Chandra* telescope provides the best data to date of any X-ray halo, while the energy range and resolution allow us to explore the halo’s behavior above 2 keV as a function of energy. The biggest surprise of this observation is the apparent additional energy-dependence of the halo. While we cannot with certainty say this is either astrophysical in origin or due to calibration issues, we plan future study of the effect. Despite this uncertainty, a number of issues are clear from these results.

We have found that models with “fluffy” dust are not required by this data. The X-ray halo surface brightness is proportional to $N_{\text{H}} \times \rho^2$. At most, the true column density to GX 13+1 is only twice the value determined from these halo observations, which allows for a dust grain density at most 30% lower than the nominal value. A “fluffy” dust model may exist that matches the observations, but it would have to include substantially more dust grains to maintain the total scattering cross section. For example, an MRN-type model with $\rho = \rho_{\text{MRN}}/5$ would need 25 times more dust to achieve the same total scattering.

At the same time, the large dust grain model used in Witt, Smith & Dwek (2001) is also not supported by these data, in agreement with the results of Predehl & Schmitt (1995). The large dust grains cause the scattering at very small observed angles ($< 100''$) to increase dramatically. The ROSAT PSPC data used by Witt, Smith & Dwek (2001) had only one point at $100''$, which drove the fit to prefer the large dust grain model. *Chandra*'s superior angular and energy resolution (and range) show that for this line of sight at least, large dust grains are not significant.

We would like to thank Terry Gaetz, Diab Jerius, and Eli Dwek for many helpful discussions. We were supported by the Chandra X-ray Science Center and NASA Chandra observation grant GO0-1107X.

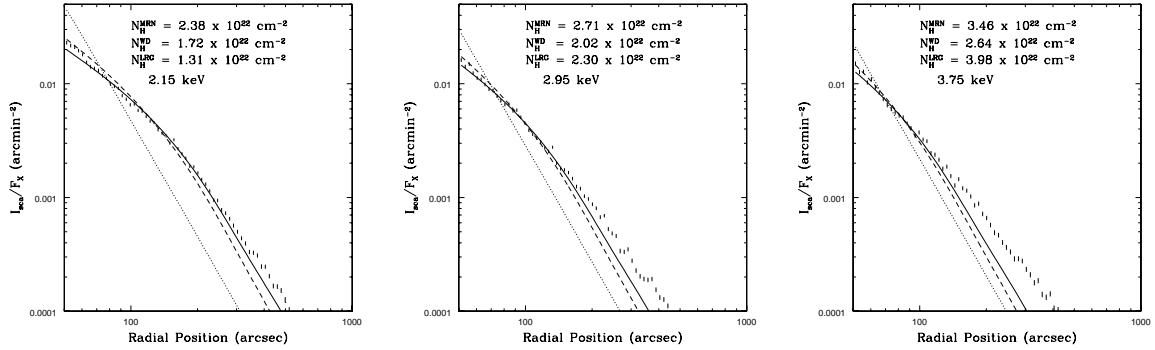


Fig. 4.— X-ray halos observed at 2.15 ± 0.1 , 2.95 ± 0.1 , and 3.75 ± 0.1 keV, fit using smoothly-distributed dust described by the MRN (solid line), WD (dashed line), and the XMRN models. The only free parameter N_{H} differs substantially between the three grain models, and it appears to increase with X-ray energy for all three models.

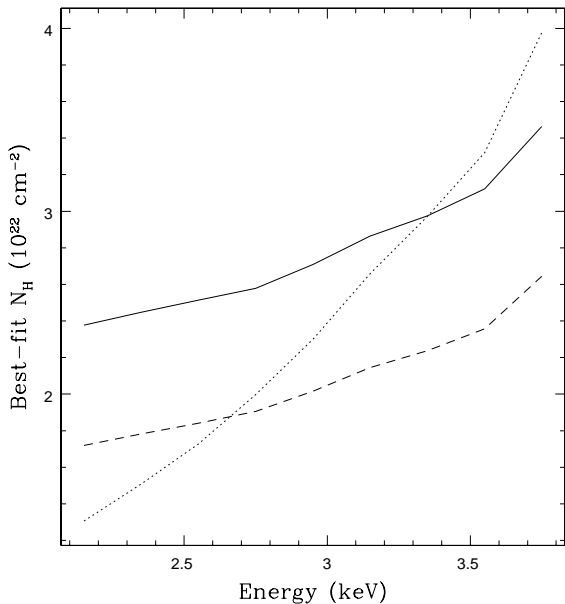


Fig. 5.— The best-fit N_{H} as a function of X-ray energy both for the MRN model (solid line) and the WD model (dashed line). The increase, although relatively small, is clear in both cases. The statistical error bars (not shown) are on order 1%; the actual error is dominated by calibration uncertainties.

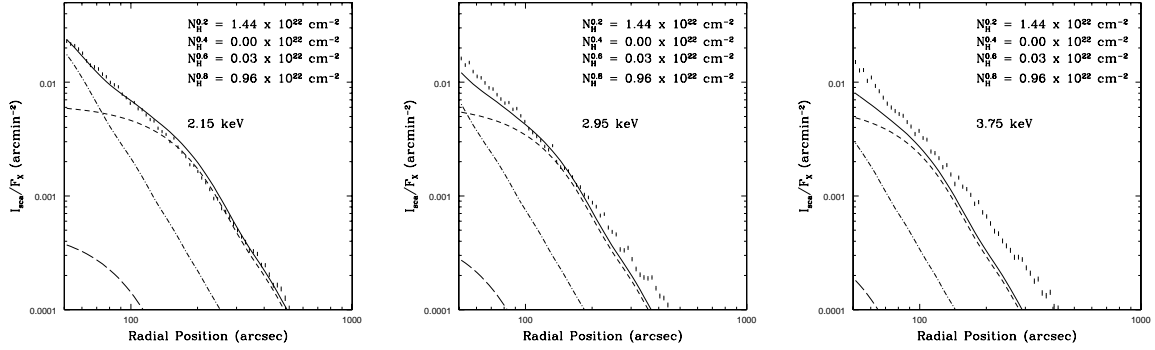


Fig. 6.— X-ray halos observed at 2.15 ± 0.1 , 2.95 ± 0.1 , and 3.75 ± 0.1 keV, fit using four evenly-spaced clouds of dust (using an MRN model) at 20%, 40%, 60%, and 80% of the distance to GX 13+1. Each dust cloud has a variable amount of dust parameterized by N_H . The best-fit total scattering is given by the solid line. The scattering from the cloud at 20% is shown by the dashed line, at 60% by the long-dashed line, and at 80% by the dot-dashed line.

REFERENCES

Bandyopadhyay, R. M., Shahbaz, T., Charles, P. A. & Naylor, T. 1999, MNRAS, 306, 417

Berendsen, S. G. H., Fender, R., Kuulkers, E., Heise, J. & van der Klis, M. 2000, MNRAS, 318, 599

Caswell, J. L. & Haynes, R. F. 1987, A&A, 171, 261

Catura, R. C. 1983, ApJ, 275, 645

Christian, D. J. & Swank, J. H. 1997, ApJS, 109, 177

Draine, B. T. & Lee, H. M. 1984, ApJ, 285, 89

Garcia, M. R., Grindlay, J. E., Bailyn, C. D., Pipher, J. L., Shure, M. A., & Woodward, C. E. 1992, AJ, 103, 1325

Hasinger, G. & van der Klis, M. 1989, A&A, 225, 79.

Homan, J., van der Klis, M., Wijnands, R., Vaughan, B. & Kuulkers, E. 1998, ApJL, 499, L41

Landgraf, M., Baggaley, W. J., Grün, E., Kröger, H., & Linkert, G. 2000 J. Geophys. Res., 105, 10343

Mathis, J. S. & Lee, C. W. 1991, ApJ, 376, 490 (ML91)

Mathis, J. S., Cohen, D., Finley, J. P., & Krautter, J. 1995, ApJ, 449, 320

Mathis, J. S., Rumpl, W. & Nordsieck, K. H. 1977, ApJ, 217, 425 (MRN)

Mauche, C. W. & Gorenstein, P. 1986, ApJ, 302, 371

Mitsuda *et al.* 1984, PASJ, 36, 741

Makishima *et al.* 1986, ApJ308, 635

Overbeck, J. W. 1965, ApJ, 141, 864

Predehl, P. & Schmitt, J. H. H. M. 1995, A&A, 246, L40

Seward, F. D. 2000, in Allen’s Astrophysical Quantities, ed. A. N. Cox. (New York: AIP), 183

Smith, R. K. & Dwek, E. 1998, ApJ, 503, 831

Taylor, J. H. & Cordes, J. M. 1993, ApJ, 411, 674

Ueda, Y., Asai, K., Yamaoka, K., Dotani, T., & Inoue, H. 2001, ApJ, 556, L87

Weingartner, J. C. & Draine, B. T. 2001, ApJ, 548, 296

Witt, A., Smith, R. K. & Dwek, E. 2001, ApJ, 550, 201